Direct imaging of antiferromagnetic domains in Mn_2Au manipulated by high magnetic fields

A. A. Sapozhnik,[1,2] M. Filianina,[1,2] S. Yu. Bodnar,[1] A. Lamirand,[3] M.-A. Mawass,[4] Y. Skourski,[5] H.-J. Elmers,[1,2] H. Zabel,[1,2] M. Kläui,[1,2] and M. Jourdan[1,2]

[1]*Institut für Physik, JGU Mainz, Staudingerweg 7, 55128 Mainz, Germany*

[2]*Graduate School Materials Science in Mainz, Staudingerweg 9, 55128 Mainz, Germany*

[3]*Diamond Light Source, Chilton, Didcot, Oxfordshire, OX11 0DE, United Kingdom*

[4]*Helmholtz-Zentrum Berlin für Materialien und Energie, Albert-Einstein Str. 15, 12489, Berlin, Germany*

[5]*Hochfeld-Magnetlabor Dresden (HLD-EMFL), Helmholtz-Zentrum Dresden-Rossendorf, 01328 Dresden, Germany*

(Received 17 February 2018; published 27 April 2018)

In the field of antiferromagnetic (AFM) spintronics, information about the Néel vector, AFM domain sizes, and spin-flop fields is a prerequisite for device applications but is not available easily. We have investigated AFM domains and spin-flop-induced changes of domain patterns in $Mn_2Au(001)$ epitaxial thin films by x-ray magnetic linear dichroism photoemission electron microscopy (PEEM) using magnetic fields up to 70 T. As-prepared Mn_2Au films exhibit AFM domains with an average size $\leqslant 1\mu$m. Application of a 30 T field, exceeding the spin-flop field, along a magnetocrystalline easy axis dramatically increases the AFM domain size with Néel vectors perpendicular to the applied field direction. The width of Néel-type domain walls (DW) is below the spatial resolution of the PEEM and therefore can only be estimated from an analysis of the DW profile to be smaller than 80 nm. Furthermore, using the values for the DW width and the spin-flop field, we evaluate an in-plane anisotropy constant ranging between 1 and 17 eV/f.u..

DOI: 10.1103/PhysRevB.97.134429

I. INTRODUCTION

In antiferromagnetic (AFM) spintronics, ferromagnets (FM) are replaced by AFMs as active device materials [1–5]. This approach takes advantage of the fast THz dynamics of antiferromagnets, which is driven by exchange interaction. This, in principle, enables writing speeds superior to those in conventional spintronics based on FM. Additionally, the absence of a net magnetization in AFMs results in vanishing dipolar interactions, allowing for an increased information density and a high stability against disturbing external fields.

In AFM spintronics, information is encoded by the direction of the Néel vector, which is defined by the vectorial difference of the sublattice magnetizations. For spintronic applications, one requires efficient methods for reading and changing the Néel vector orientation (writing). In case of AFMs with non-centrosymmetric magnetic sublattices, it was predicted that a current-induced spin-orbit torque can change the orientation of the Néel vector [6]. This was indeed recently demonstrated for the compounds CuMnAs [7,8] and Mn_2Au [9,10]. However, the necessary current densities are, in general, close to the destruction limit and further materials optimization is required, specifically aiming at a reduced domain wall (DW) pinning. To this end, the characterization of the AFM domain structure is of major importance. Whereas x-ray magnetic linear dichroism photoemission electron microscopy (XMLD-PEEM) was successfully used to observe AFM domains and their manipulation in CuMnAs thin films [7,11], no such experiments have been reported for Mn_2Au yet. Moreover, information about the magnetocrystalline anisotropy determining the switching current [6] is required for lowering its threshold density.

Magnetic domains in different AFMs were widely studied by XMLD-PEEM during the last two decades [7,12–15]. The common procedure developed for obtaining XMLD contrast in oxides is to calculate the asymmetry from images taken at two energies corresponding to multiplet peaks of a magnetic atom. Typical domain sizes observed in oxide AFM are in the micrometer regime [12–14]. However, conductive materials, like Mn_2Au, exhibit broader x-ray absorption spectra (XAS) without multiplet structure [16]. This renders the selection of the appropriate x-ray energies for obtaining sufficient magnetic contrast challenging [17].

To understand Mn_2Au and to use this material for future devices, one needs to be able to visualize the magnetic domain configuration and to obtain key magnetic properties, such as the anisotropy constants, which are currently unknown. We report on the visualization of AFM domains in Mn_2Au epitaxial thin films using high-resolution XMLD-PEEM. We observe the alignment of the Néel vector by the application of a high magnetic field resulting in a spin-flop transition. This allows us to evaluate the magnetic in-plane anisotropy constant of Mn_2Au based on an analysis of the AFM DW width and on the spin-flop field.

II. METHODS

Epitaxial thin-film samples with a stacking sequence of $Al_2O_3(1\bar{1}02)$ substrate/Ta(001) 30 nm/Mn_2Au(001) 240 nm/AlO_x 2 nm were grown by radio frequency magnetron sputtering. The in-plane epitaxial relation as determined by x-ray diffractometry (XRD) is Ta(001)[100] $\parallel$ $Mn_2Au(001)[100]$. AlO_x capping was used as an oxidation protection. More details on the sample preparation and characterization can be found in Ref. [18].

The samples were exposed to high pulsed magnetic fields aiming at an alignment of the Néel vector by a spin-flop

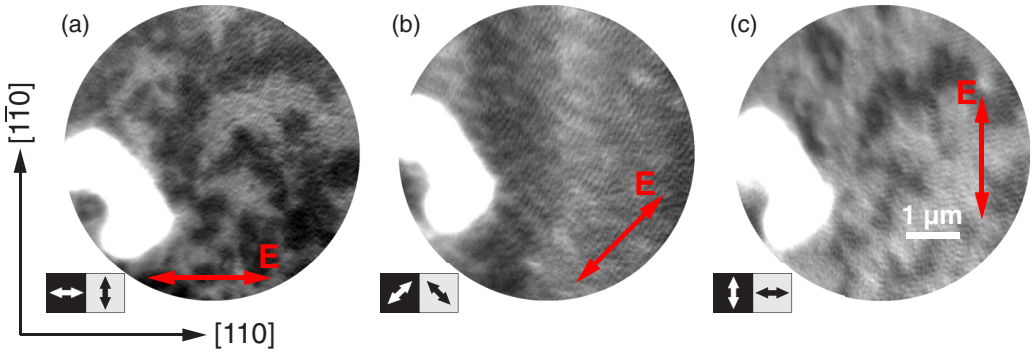

FIG. 1. Asymmetry images of the as-prepared sample. The in-plane angle of the x-ray direction of incidence is (a) 0°, (b) 45°, and (c) 90° with respect to the crystallographic [1$\bar{1}$0] axis. The red double-headed arrow indicates the electric field vector E of the linearly polarized x-ray beam. The double box at the bottom specifies the Néel vector orientation in the AFM domains. The bright area on the left-hand side of the image is caused by the marker, which was used to keep the image position fixed during rotation of the sample.

transition. Magnetic fields of different amplitudes ranging from 30 T to 70 T were applied along the [110] and [100] directions of Mn_2Au at room temperature at the High Magnetic Field Laboratory of the Helmholtz-Zentrum Dresden-Rossendorf (HZDR), Germany.

The XMLD-PEEM studies were performed at beamline I06 at Diamond Light Source, UK, and with the SPEEM setup at BESSY II, Helmholtz-Zentrum Berlin (HZB), Germany. Both instruments are equipped with Elmitec photoemission electron microscopes providing ∼50 nm spatial resolution and 0.4 eV energy resolution. The x-ray beam, linearly polarized in the sample plane, was incident under an angle of 16° to the sample surface. Controllable rotation procedures guaranteed measurements within the same area on the surface at different rotation angles around the sample normal. The strongest in-plane magnetic contrast was achieved by calculating the asymmetry of two images taken at x-ray energies E_{MAX} and E_{MIN}, at which the maximum and the minimum of a previously measured XMLD spectrum was obtained [16]:

$$I_{asym} = \frac{I(E_{MAX}) - I(E_{MIN})}{I(E_{MAX}) + I(E_{MIN})}. \quad (1)$$

The XAS was determined from a set of images obtained in a range of energies close to the L_3 absorption edge of Mn. The absorption coefficient was calculated as the sum of grayscale levels over a region of interest in the center of the field of view.

In our previous work, we measured the absorption spectrum of Mn_2Au [16] and demonstrated that E_{MAX} and E_{MIN} are separated by 0.8 eV and 0.0 eV from the L_3 absorption edge, respectively. This information, in combination with the XAS determined from the images as discussed above, was used for defining E_{MAX} and E_{MIN} for each sample.

III. EXPERIMENTAL RESULTS AND DISCUSSION

The as-prepared sample not exposed to a high magnetic field exhibits small contrast features with an average size of $\sim 1\mu$m in the asymmetry image [Fig. 1(a)]. The contrast disappears when the sample (corresponding to the direction of x-ray incidence) is rotated by 45° [Fig. 1(b)] and reverses after 90° rotation of the sample [Fig. 1(c)], which demonstrates the magnetic origin of the observed asymmetry. From the vanishing contrast of Fig. 1(b) and the appearance of basically two levels of gray in Figs. 1(a) and 1(c), we conclude that the Néel vector is always oriented parallel to the ⟨110⟩ directions, which is consistent with the reported easy axes of Mn_2Au [19,20]. Thus, the as-prepared Mn_2Au sample shows an AFM domain pattern as displayed in Fig. 1 with an average domain size of $\sim 1\mu$m. Moreover, the parts of the sample covered with the two energetically equivalent domains with 90° different Néel vector orientations are comparable.

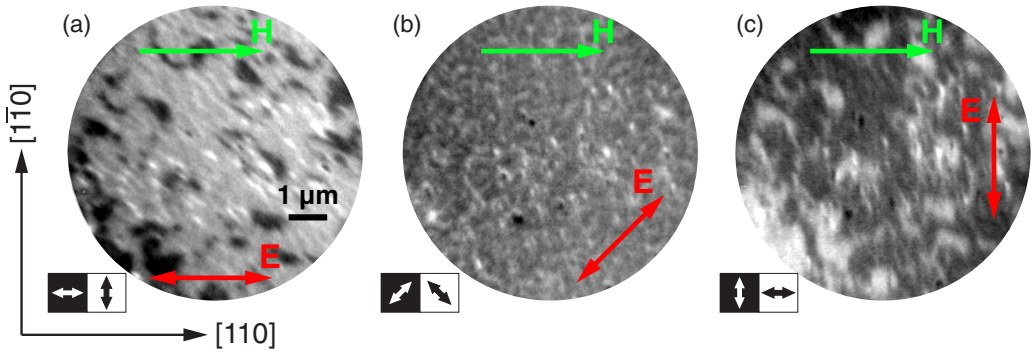

FIG. 2. Asymmetry images of a Mn_2Au sample after exposure to a magnetic field of 30 T along the [110] direction (green arrow). The in-plane angle of the x-ray direction of incidence is (a) 0°, (b) 45°, and (c) 90°. The red double-headed arrow indicates the polarization of the linearly polarized x-ray beam. The double box at the bottom specifies the Néel vector orientation within the AFM domains.

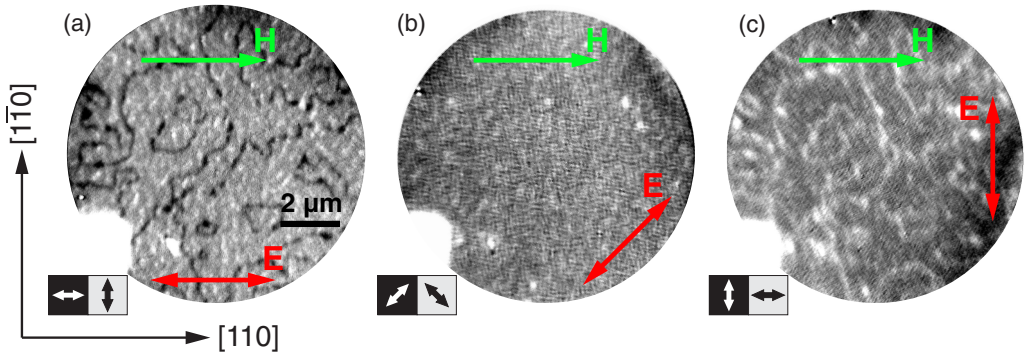

FIG. 3. Asymmetry images of a Mn_2Au sample after exposure to a magnetic field of 50 T along the [110] direction (green arrow). The in-plane angle of the x-ray direction of incidence is (a) 0°, (b) 45°, and (c) 90°. The red double-headed arrow indicates the polarization of the linearly polarized x-ray beam. The double box at the bottom specifies the Néel vector orientation within the AFM domains.

Having established the as-grown domain structure, the next step is to study changes in the domain structure when the AFM is exposed to magnetic fields sufficiently high to potentially manipulate the AFM. Figure 2 shows XMLD-PEEM images of a sample exposed to a 30 T external field along the [110] direction, which is an easy axis of the material. A strong magnetic contrast in the asymmetry image appears for the x-ray incidence direction (surface projected) parallel to [1$\bar{1}$0] (0°), which displays large bright (light gray) areas with minor dark inclusions [Fig. 2(a)]. Again, the contrast reverses upon rotation of the sample by 90° with respect to the direction of x-ray incidence [Fig. 2(c)], demonstrating the magnetic origin of the asymmetry. Please note that the magnetic contrast vanishes upon rotation by 45° leaving only some morphology-related features visible [Fig. 2(b)]. A field of 30 T significantly increases the size of domains with the Néel vector perpendicular to the field. This phenomenon can be explained by a spin-flop transition, which results in a reorientation of the Néel vector perpendicular to the direction, in which the magnetic field was applied. We conclude that the majority of the AFM spin structure has been aligned with the axis favored by the spin-flop transition. From this, we deduce an upper bound for the spin-flop field of our Mn_2Au thin films of 30 T.

A higher magnetic field of 50 T applied along the [110] direction causes a similar reorientation of the domain structure (Fig. 3). The asymmetry image shows bright (light gray) areas separated by narrow, wormlike dark lines [Fig. 3 (a)]. Due to their average width of $\sim$ 100 nm, a higher resolution for resolving the spin structure within them would be required. The dark lines can either be magnetic domains with the Néel vector oriented along the [110] direction or can be considered 180° DWs. The presence of not closed lines can be seen as evidence against the DW hypothesis. However, the gaps in the black lines can be caused by the surface morphology contributing to the asymmetry via, e.g., residual drifts in the images remaining even after corrections.

Finally, we probe the effect of a 70 T external field applied along the [100] axis of Mn_2Au, which is a hard magnetic direction (Fig. 4). The AFM domain structure is decomposed into domains with an average size of $\sim$1 to 3 μm, which typically have a different shape compared to the as-prepared sample. However, the proportion of both types of AFM domains is equal, indicating no preferred Néel vector orientation on a large scale.

This observation is explained by the fact that a high enough external field applied along the hard [100] axis orients the Néel vector along the perpendicular [010]-hard axis. When the field is reduced, the moments redistribute themselves parallel to the easy axes creating a new domain pattern. This leads to a slight increase of the average domain size in comparison to the as-prepared state shown in Fig. 1. These results confirm ⟨110⟩ to be the easy axes of our Mn_2Au thin films [19,20].

The upper boundary identified for the field required to generate a spin-flop transition allows us to determine the in-plane anisotropy constant (H_a^{IP}) of Mn_2Au(001) utilizing the following expression for the spin-flop field $H_{\mathrm{SF}} = \sqrt{2H_{\mathrm{ex}}H_a^{\mathrm{IP}}}$ [21]. Using the exchange field from Ref. [22] to be $\mu_0 H_{\mathrm{exch}} = 1300$ T, we find an upper boundary of $\mu_0 H_a^{\mathrm{IP}} = 0.35$ T. Adopting the expression for the in-plane anisotropy $K_4 \sin^4\theta \cos(4\phi)$ from Ref. [19], the derived anisotropy field corresponds to the maximal value of $K_{4\parallel} \leqslant 17\,\mu$eV/f.u., which is in line with theoretical predictions of 10 eV/f.u. [19].

IV. DETERMINATION OF THE DOMAIN-WALL WIDTH IN Mn_2Au

Due to a high c-axis magnetocrystalline anisotropy in Mn_2Au [19], in-plane (Néel type) DWs are energetically more favorable in our thin films than Bloch walls with an out-of-plane component. The intrinsic DW width can be

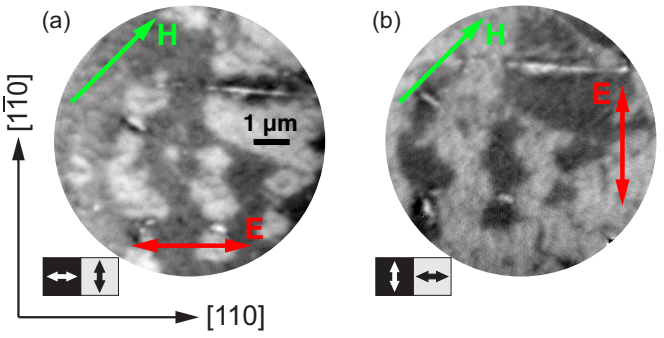

FIG. 4. Asymmetry images of a Mn_2Au sample after exposure to a magnetic field of 70 T along the [100] direction (green arrow). The in-plane angle of the x-ray direction of incidence is (a) 0°, (b) 90°. The red double-headed arrow indicates the polarization of the linearly polarized x-ray beam. The double box at the bottom specifies the Néel vector orientation within the AFM domains.

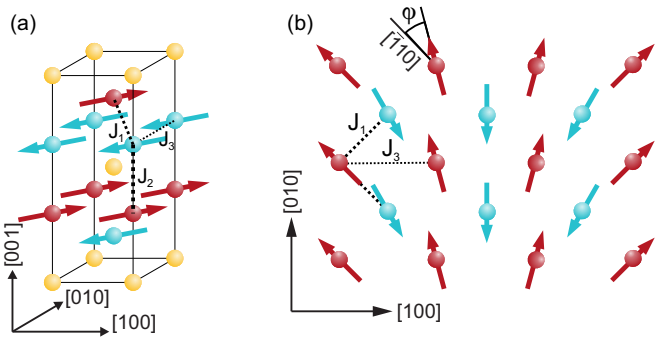

FIG. 5. (a) Unit cell of Mn_2Au indicating the exchange constants. (b) Schematic representation of a Néel-type domain wall viewed along the [001] axis.

determined by minimizing the total DW energy per unit area, which contains exchange interaction and magnetocrystalline anisotropy terms [23]:

$$E[\phi(x)] = \int_{-\infty}^{\infty} \left(Ja^2 \left(\frac{d\phi}{dx} \right)^2 + K_4(1 - \cos 4\phi) \right) n \, dx, \tag{2}$$

where $J = \frac{1}{4}(J_1 + 2J_3)$ [see Fig. 5(a)] for [100] DWs [see Fig. 5(b)], K_4 is the fourfold anisotropy constant, n is the volume density of Mn atoms, and a is the Mn_2Au lattice constant. The choice of the anisotropy term corresponds to the angle ϕ between the [$\bar{1}$10] easy axis and the staggered magnetization direction [Fig. 5 (b)]. The solution of the variational problem for the functional in Eq. (2) with the boundary conditions $\phi(-\infty) = 0$ and $\phi(\infty) = \pi/2$ provides the DW profile:

$$\phi_{[100]}(x) = \arctan \, \exp \left(\sqrt{\frac{8K_4}{Ja^2}} x \right). \tag{3}$$

The DW width can be expressed by the slope of $\phi(x)$ at $x = 0$, i.e., in the center of the DW. Using Eq. (3), the 90° DW width is derived as

$$w = \frac{\pi}{2} \frac{1}{d\phi_{[100]}(x)/dx(x = 0)} = \frac{\pi}{2} \sqrt{\frac{J}{2K_4}} a. \tag{4}$$

Please note that similar considerations apply for determining the width of [110] DWs, resulting in the same expression Eq. (4).

Since the XMLD does not change sign upon Néel vector inversion, the normalized XMLD-PEEM contrast across a DW is proportional to the squared cosine of the angle between the Néel vector and the x-ray electric field $I_{DW}(x) \propto \cos^2 \phi(x)$ [24]. Thus, in analogy with Eq. (4), the AFM DW width observed in the experiment is

$$w_{exp} = \frac{1}{dI_{DW}(x)/dx(x = 0)} = \sqrt{\frac{J}{2K_4}} a. \tag{5}$$

This result indicates that a DW appears $\pi/2$ times more narrow in an XMLD-PEEM image in comparison with the actual width.

However, in an XMLD-PEEM experiment, the DW image is broadened due to the finite instrumental resolution, which can be represented as Gaussian function ($Res_\sigma(x)$), with the parameter 2σ defining the resolution. For the determination of 2σ, an intensity profile was measured across the edge of the defect in the top right part of Fig. 4(a) [blue line in Fig. 6(a)]. Each point is averaged over 150 nm perpendicular to the line. The profile was fitted by the Gaussian error function [Fig. 6(b)], which is a convolution of the step function and of the Gaussian function. We obtain $2\sigma \simeq 47$ nm.

A DW profile was determined across a straight section of a domain wall [green line in Fig. 6(a)] with every point averaged over 300 nm perpendicular to the line, as depicted in Fig. 6(c). The profile was fitted by a convolution of the instrumental resolution function and of the determined DW profile $(I_{DW} * Res_\sigma)(x)$ with the fit parameter $2K_4/J$. The value of $2K_4/J$ providing the best fit is 2×10^{-4}. Additionally, we estimated a lower limit of this parameter of 0.5×10^{-4} [see Fig. 6(c)]. Based on Eq. (4), this value corresponds to an upper limit for the DW width of 80 nm, which is of the same order of magnitude as the instrumental resolution. Please note that our analysis relies on the assumption of a perfect straight DW section. In FM thin films, straight DW sections are favored, minimizing stray fields, which are absent in AFM. Therefore, the apparently straight DW section in an AFM might show a variation of the position perpendicular to the profile. Considering the expected DW width, a much higher

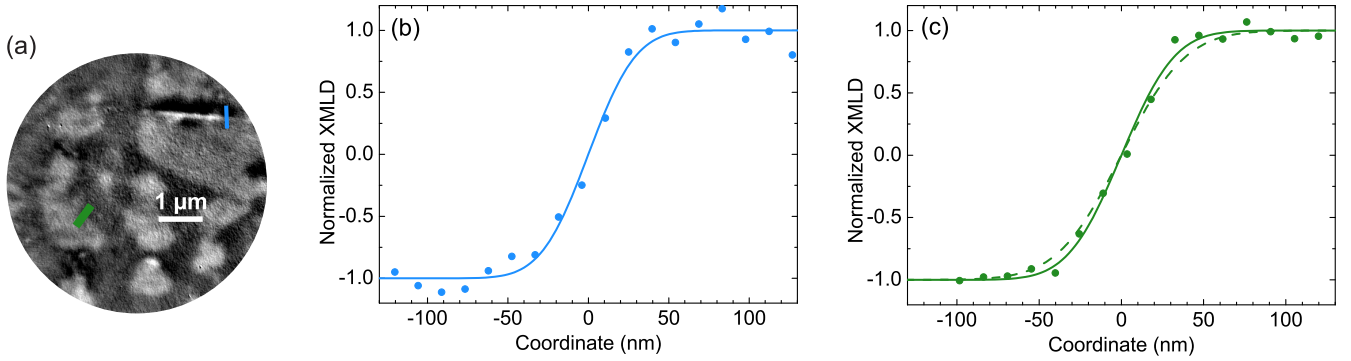

FIG. 6. (a) Reproduction of Fig. 4(a) with indicated paths used for measuring the line profiles. (b) Line profile across the topographical structure indicated by the blue line in (a) and corresponding fit with a Gaussian error function. (c) Line profile across the straight domain wall section indicated by the green line in (a) and fits corresponding to $2K_4/J = 2 \times 10^{-4}$ (solid line) and $2K_4/J = 0.5 \times 10^{-4}$ (dashed line).

spatial resolution of better than 10 nm is necessary for detailed investigations of DWs in Mn_2Au.

Finally, the DW width provides an additional estimate of the anisotropy constant K_4. Using $J = 13.5$ meV from Ref. [25], we find $K_4 = 1$ μeV/f.u. This value is the lower boundary for the in-plane anisotropy constant corresponding to an anisotropy field of 0.02 T and $H_{SF} = 7$ T.

V. CONCLUSIONS

Using XMLD-PEEM, we obtained images of AFM domains in Mn_2Au thin-film samples. The easy axis was experimentally determined to be parallel to the crystallographic ⟨110⟩ directions, in agreement with reports on bulk single crystals. A typical AFM domain size of $\simeq 1$ μm was observed for as-grown thin films.

AFM domains were manipulated by a large magnetic field of 30 T, generating a spin-flop transition. From the magnitude of this field, we estimate an in-plane magnetic anisotropy constant $K_4 \leqslant 17$ μeV/f.u. Samples exposed to a large magnetic field along the [110] easy axis show large AFM domains with the Néel vector oriented primarily perpendicular to the field. A strong magnetic field directed along the [100] hard axis results in a slight increase of the size and in a modification of the shape of the domains, preserving almost equal proportion of in-plane Mn_2Au domains oriented along the two easy axes.

A detailed analysis of the measured DW profiles indicates a DW width smaller than 80 nm, which is at the limit of the instrumental resolution. Nevertheless, this value can be used to estimate a lower limit of K_4 of 1 μeV/f.u.. From the combination of both limits, we estimate a value of the anisotropy constant K_4 between 1 and 17 μeV/f.u..

ACKNOWLEDGMENTS

The research was financially supported by the German Research Foundation (Deutsche Forschungsgemeinschaft) through the Transregional Collaborative Research Center 173 Spin+X, Project No. A05. A.A.S. also wishes to acknowledge the fellowship of the MAINZ Graduate School of Excellence. We thank the Diamond Light Source for the allocation of beam time under Proposal No. SI17120-1 and HZB for the allocation of beam time under Proposal No. 17206035-ST. We acknowledge the support of the Hochfeld-Magnetlabor Dresden (HLD) at HZDR, member of the European Magnetic Field Laboratory (EMFL).

[1] A. H. MacDonald and M. Tsoi, Philos. Trans. Royal Soc. A **369**, 3098 (2011).
[2] O. Gomonay, T. Jungwirth, and J. Sinova, Phys. Status Solidi RRL **11**, 1700022 (2017).
[3] E. V. Gomonay and V. M. Loktev, Low Temp. Phys. **40**, 17 (2014).
[4] T. Jungwirth, X. Marti, P. Wadley, and J. Wunderlich, Nat. Nanotechnol. **11**, 231 (2016).
[5] V. Baltz, A. Manchon, M. Tsoi, T. Moriyama, T. Ono, and Y. Tserkovnyak, Rev. Mod. Phys. **90**, 015005 (2018).
[6] J. Železný, H. Gao, K. Výborný, J. Zemen, J. Mašek, A. Manchon, J. Wunderlich, J. Sinova, and T. Jungwirth, Phys. Rev. Lett. **113**, 157201 (2014).
[7] P. Wadley, B. Howells, J. Železný, C. Andrews, V. Hills, R. P. Campion, V. Novák, K. Olejník, F. Maccherozzi, S. S. Dhesi, S. Y. Martin, T. Wagner, J. Wunderlich, F. Freimuth, Y. Mokrousov, J. Kuneš, J. Chauhan, M. J. Grzybowski, A. W. Rushforth, K. W. Edmonds, B. L. Gallagher, and T. Jungwirth, Science **351**, 587 (2016).
[8] K. Olejník, V. Schuler, X. Marti, V. Novák, Z. Kašpar, P. Wadley, R. P. Campion, K. W. Edmonds, B. L. Gallagher, J. Garces, M. Baumgartner, P. Gambardella, and T. Jungwirth, Nat. Commun. **8**, 15434 (2017).
[9] S. Yu. Bodnar, L. Šmejkal, I. Turek, T. Jungwirth, O. Gomonay, J. Sinova, A. A. Sapozhnik, H.-J. Elmers, M. Kläui, and M. Jourdan, Nat. Commun. **9**, 348 (2018).
[10] M. Meinert, D. Graulich, and T. Matalla-Wagner, arXiv:1706.06983 [cond-mat].
[11] P. Wadley, S. Reimers, M. J. Grzybowski, C. Andrews, M. Wang, J. S. Chauhan, B. L. Gallagher, R. P. Campion, K. W. Edmonds, S. S. Dhesi, F. Maccherozzi, V. Novak, J. Wunderlich, and T. Jungwirth, Nat. Nanotechnol. (2018), doi: 10.1038/s41565-018-0079-1.
[12] J. Stöhr, A. Scholl, T. J. Regan, S. Anders, J. Lüning, M. R. Scheinfein, H. A. Padmore, and R. L. White, Phys. Rev. Lett. **83**, 1862 (1999).
[13] F. Nolting, A. Scholl, J. Stöhr, J. W. Seo, J. Fompeyrine, H. Siegwart, J.-P. Locquet, S. Anders, J. Lüning, E. E. Fullerton, M. F. Toney, M. R. Scheinfein, and H. A. Padmore, Nature(London) **405**, 767 (2000).
[14] I. P. Krug, F. U. Hillebrecht, M. W. Haverkort, A. Tanaka, L. H. Tjeng, H. Gomonay, A. Fraile-Rodríguez, F. Nolting, S. Cramm, and C. M. Schneider, Phys. Rev. B **78**, 064427 (2008).
[15] L. Baldrati, A. Ross, T. Niizeki, C. Schneider, R. Ramos, J. Cramer, O. Gomonay, M. Filianina, T. Savchenko, D. Heinze, A. Kleibert, E. Saitoh, J. Sinova, and M. Kläui, arXiv:1709.00910 [cond-mat].
[16] A. A. Sapozhnik, R. Abrudan, Y. Skourski, M. Jourdan, H. Zabel, M. Kläui, and H.-J. Elmers, Phys. Status Solidi RRL **11**, 1600438 (2017).
[17] M. J. Grzybowski, P. Wadley, K. W. Edmonds, R. Beardsley, V. Hills, R. P. Campion, B. L. Gallagher, J. S. Chauhan, V. Novak, T. Jungwirth, F. Maccherozzi, and S. S. Dhesi, Phys. Rev. Lett. **118**, 057701 (2017).
[18] M. Jourdan, H. Bräuning, A. Sapozhnik, H.-J. Elmers, H. Zabel, and M. Kläui, J. Phys. D: Appl. Phys. **48**, 385001 (2015).
[19] A. B. Shick, S. Khmelevskyi, O. N. Mryasov, J. Wunderlich, and T. Jungwirth, Phys. Rev. B **81**, 212409 (2010).
[20] V. M. T. S. Barthem, C. V. Colin, R. Haettel, D. Dufeu, and D. Givord, J. Magn. Magn. Mater. **406**, 289 (2016).
[21] F. L. A. Machado, P. R. T. Ribeiro, J. Holanda, R. L. Rodríguez-Suárez, A. Azevedo, and S. M. Rezende, Phys. Rev. B **95**, 104418 (2017).
[22] V. M. T. S. Barthem, C. V. Colin, H. Mayaffre, M.-H. Julien, and D. Givord, Nat. Commun. **4**, 2892 (2013).
[23] T. Yamada, J. Phys. Soc. Jpn. **21**, 650 (1966).
[24] D. Alders, J. Vogei, C. Levelut, S. D. Peacor, T. Hibma, M. Sacchi, L. H. Tjeng, C. T. Chen, G. van der Laan, B. T. Thole, and G. A. Sawatzky, Europhys. Lett. **32**, 259 (1995).
[25] S. Khmelevskyi and P. Mohn, Appl. Phys. Lett. **93**, 162503 (2008).